Journal of Biomedical Optics

BiomedicalOptics.SPIEDigitalLibrary.org

Backscattering of linearly polarized light from turbid tissue-like scattering medium with rough surface

Alexander Doronin
Lioudmila Tchvialeva
Igor Markhvida
Tim K. Lee
Igor Meglinski

SPIE.

Alexander Doronin, Lioudmila Tchvialeva, Igor Markhvida, Tim K. Lee, Igor Meglinski, "Backscattering of linearly polarized light from turbid tissue-like scattering medium with rough surface," *J. Biomed. Opt.* **21**(7), 071117 (2016), doi: 10.1117/1.JBO.21.7.071117.

Backscattering of linearly polarized light from turbid tissue-like scattering medium with rough surface

Alexander Doronin,[a] Lioudmila Tchvialeva,[b] Igor Markhvida,[b] Tim K. Lee,[b,c,d] and Igor Meglinski[e,*]
[a]Yale University, Department of Computer Science, Computer Graphics Group, New Haven 06511, United States
[b]University of British Columbia and Vancouver Coastal Health Research Institute, Department of Dermatology and Skin Science, Photomedicine Institute, Vancouver V5Z 4E8, Canada
[c]BC Cancer Agency, Departments of Cancer Control Research and Integrative Oncology, Vancouver V5Z 1L3, Canada
[d]Simon Fraser University, School of Computing Science, Burnaby V5A 1S6, Canada
[e]University of Oulu, Opto-Electronics and Measurement Techniques Laboratory, Oulu FI-9014, Finland

Abstract. In the framework of further development of a unified computational tool for the needs of biomedical optics, we introduce an electric field Monte Carlo (MC) model for simulation of backscattering of coherent linearly polarized light from a turbid tissue-like scattering medium with a rough surface. We consider the laser speckle patterns formation and the role of surface roughness in the depolarization of linearly polarized light backscattered from the medium. The mutual phase shifts due to the photons' pathlength difference within the medium and due to reflection/refraction on the rough surface of the medium are taken into account. The validation of the model includes the creation of the phantoms of various roughness and optical properties, measurements of co- and cross-polarized components of the backscattered/reflected light, its analysis and extensive computer modeling accelerated by parallel computing on the NVIDIA graphics processing units using compute unified device architecture (CUDA). The analysis of the spatial intensity distribution is based on second-order statistics that shows a strong correlation with the surface roughness, both with the results of modeling and experiment. The results of modeling show a good agreement with the results of experimental measurements on phantoms mimicking human skin. The developed MC approach can be used for the direct simulation of light scattered by the turbid scattering medium with various roughness of the surface. [DOI: 10.1117/1.JBO.21.7.071117]

Keywords: polarized light; rough surface; backscattering; Monte Carlo modeling; turbid media; depolarization.

Paper 140856SSRRR received Dec. 23, 2014; accepted for publication Jun. 14, 2016; published online Jul. 11, 2016.

1 Introduction

The last decade has seen growing interest to the propagation of coherent polarized light in turbid tissue-like scattering media.[1,2] The majority of recent studies associated with the polarized light are focused on the development of new diagnostic modalities for noninvasive characterization of biological tissues with the special attention to cancer screening.[3,4] The incident polarized light is multiply scattered along its propagation within the biological tissue and becomes depolarized. The depolarization ratio (DR) depends strongly on the size and shape of scattering particles,[5,6] as well as on the number of scattering events,[7,8] and is independent of the state of polarization of incident light.[9] Thus, scattering properties of a turbid medium can be evaluated quantitatively by monitoring the evolution of the polarization state of scattered light in comparison with the polarization of incident light. The Mueller matrix approach is typically utilized to assess the properties of the medium based on polarization measurements.[2] Potentially, this approach can be used for noninvasive cancer diagnosis, e.g., for colon cancer detection.[10] In fact, typically utilized in diagnostic practice, the backscattered polarized light contains not only the light scattered within the medium but also the light reflected by the surface of the medium. Presently, there is an escalating interest in the surface roughness that potentially can be used in cancer diagnosis, e.g., for an assessment of grade of skin neoplasia.[11] To introduce a roughness score, the malignant features have been observed with the reflectance confocal microscopy.[12] Relief patterns of the skin surface of benign and malignant lesions of the skin have been studied by microtopography.[13] The polarization imaging with high angles of incidence has been extensively used in routine clinical studies of skin roughness.[14] Tchvialeva et al.[15] suggested a methodology of quantifying skin surface roughness by analyzing the laser speckle contrast of the backscattered linearly polarized light. In spite of numerous studies in the field, a clear understanding of influence of surface roughness on the formation of polarized laser speckles is still required.

In this paper, in the framework of further development of a unified computational model for the needs of biomedical optics,[16,17] we present the electric field Monte Carlo (MC) approach specially developed for simulation of backscattering of coherent polarized light from turbid tissue-like scattering media with rough surfaces. The developed computational model is based on the Jones formalism and takes into account the wave properties of light, including temporal coherence, polarization, phase change on the reflection and/or refraction at the rough medium boundary, and interference. Using the developed electric field MC approach, we explore the influence of the surface roughness on the resulted depolarization of coherent linearly polarized light backscattered from various turbid media of known optical properties, which are in order of human skin lesions. In particular, we examine the laser speckle patterns

*Address all correspondence to: Igor Meglinski, E-mail: igor.meglinski@oulu.fi

1083-3668/2016/$25.00 © 2016 SPIE

formation and dependence of DR on the surface roughness of a phantom medium.

2 Theory

2.1 *Basic Elements of Light Wave Propagation in Turbid Medium*

The concept of light as a wave is fundamental for the phenomena of coherence and polarization.[18] Coherence is a quantitative measure of the degree of phase correlation of the light wave, whereas the polarization is defined by the electric field vector $\vec{\mathbf{E}}$ lying in the plane perpendicular to the direction of the light wave propagation. The light wave with the electric field $\vec{\mathbf{E}}$ is incident normally to the surface of the medium and is propagating along the z-direction in frame of the standard Cartesian coordinate system. The complex field components with amplitudes E_{0_x}, E_{0_y} and phases φ_x, φ_y at time t are presented in terms of the two-element matrix, known as a "Jones vector"[19]

$$\vec{\mathbf{E}} = \begin{bmatrix} E_x \\ E_y \end{bmatrix} = \begin{bmatrix} E_{0_x} e^{i(kz-\omega t+\varphi_x)} \\ E_{0_y} e^{i(kz-\omega t+\varphi_y)} \end{bmatrix}, \tag{1}$$

where i is the imaginary unit, k is the wave number ($k = 2\pi/\lambda$, λ is the wavelength of incident light), ω is the angular frequency, and $\Delta\varphi = \varphi_x - \varphi_y = 0$ (i.e., linearly polarized light is considered). Absorption of light in the medium changes the amplitude of the components of the field presented in Eq. (1). The complex refractive index $\tilde{n} = n_{\mathrm{R}} + \mathrm{i}n_{\mathrm{I}}$ is used to define the complex phase shift induced by the medium

$$\vec{\mathbf{E}}_{\mathrm{out}} = \vec{\mathbf{E}}_{\mathrm{in}} e^{i\frac{2\pi}{\lambda}n_{\mathrm{R}}S} e^{-\frac{2\pi}{\lambda}n_{\mathrm{I}}S}, \tag{2}$$

where S is the trajectory of a light wave in the medium, defined as a sum of pathlengths l_i between successive scattering events, counted from the point of entrance into the medium to the point of output ($S = \sum l_i$), $\mathrm{Re}(\tilde{n}) = n_{\mathrm{R}}$ is defined by the ordinary refractive index, and the term $e^{i(2\pi/\lambda)n_{\mathrm{R}}S}$ describes the wave retarded by $(2\pi/\lambda)n_{\mathrm{R}}S$; $\mathrm{Im}(\tilde{n}) = n_{\mathrm{I}}$ is known as the extinction coefficient and determines the rate of absorption of light in the medium. The term $e^{-(2\pi/\lambda)n_{\mathrm{I}}S}$ defines the amplitude attenuation of the Jones vector components [see Eq. (1)] and is related to the well-known Beer–Lambert–Bouguer law

$$I = I_0 e^{-\mu_t S}, \tag{3}$$

where μ_t is the attenuation coefficient, $\mu_t = \mu_{\mathrm{s}} + \mu_{\mathrm{a}}$, μ_{a} is the absorption coefficient ($\mu_{\mathrm{a}} = 4\pi n_I S/\lambda$), and μ_{s} is the scattering coefficient.

The superposition of N_{ph} light waves at the detecting area for the absorption-free ($\mu_{\mathrm{a}} = 0$) medium is defined as

$$E_x^2 = \sum_{m=1}^{N_{\mathrm{ph}}} E_{0_{xm}}^2 + 2\sum_{m>v}^{N_{\mathrm{ph}}}\sum_{v=1}^{N_{\mathrm{ph}}} E_{0_{xm}} E_{0_{xv}} \cos(\alpha_v - \alpha_m) \times \exp\left[-\left(\frac{\Delta L_{m,v}}{l_{\mathrm{c}}/\sqrt{2}}\right)^2\right],$$

$$E_y^2 = \sum_{m=1}^{N_{\mathrm{ph}}} E_{0_{ym}}^2 + 2\sum_{m>v}^{N_{\mathrm{ph}}}\sum_{v=1}^{N_{\mathrm{ph}}} E_{0_{ym}} E_{0_{yv}} \cos(\alpha_v - \alpha_m) \times \exp\left[-\left(\frac{\Delta L_{m,v}}{l_{\mathrm{c}}/\sqrt{2}}\right)^2\right], \tag{4}$$

where $\alpha_{m,v} = kS_{m,v} + \phi_{m,v}$ shows the phases for x and y components, respectively, $\Delta L_{m,v}$ is the pathlength difference ($\Delta L_{m,v} = S_m - S_v$), l_{c} is the temporal coherence length of the incident light, and ϕ is the phase shift of individual waves indicated by indices m and v.

Reflection and refraction of light waves at the medium boundary are described by the Fresnel's reflection coefficients and defined for the transverse magnetic (TM) and transverse electric (TE) components (or, respectively, for x and y components) as[19]

$$R_{\mathrm{TM}} = \left|\frac{n_1 \cos\theta_{\mathrm{t}} - n_2 \cos\theta_{\mathrm{i}}}{n_1 \cos\theta_{\mathrm{t}} + n_2 \cos\theta_{\mathrm{i}}}\right|^2,$$

$$R_{\mathrm{TE}} = \left|\frac{n_1 \cos\theta_{\mathrm{i}} - n_2 \cos\theta_{\mathrm{t}}}{n_1 \cos\theta_{\mathrm{i}} + n_2 \cos\theta_{\mathrm{t}}}\right|^2, \tag{5}$$

where n_1 and n_2 are the refractive indices of the external and internal media, respectively, θ_{i} is the angles of light incidence, and θ_{t} is the angle refraction on the medium boundary. Figure 1 shows the Fresnel's reflection coefficients counted by Eq. (5) for external ($n_1 < n_2$) and internal ($n_1 > n_2$) reflection.

In the case of external reflection ($n_1 < n_2$), a π-phase shift occurs at any angle of incidence for the TE field component and for the TM field component when $\theta_{\mathrm{i}} < \theta_{\mathrm{p}}$. Here, θ_{p} is the polarizing angle at which $R_{\mathrm{TM}} = 0$, also known as Brewster's angle. For the internal reflection ($n_1 > n_2$) the phase shift is defined as[19]

$$\phi_{\mathrm{TM}} = \begin{cases} 0, & \theta_{\mathrm{i}} < \theta_{\mathrm{p}}, \\ \pi, & \theta_{\mathrm{p}} < \theta_{\mathrm{i}} < \theta_{\mathrm{c}}, \\ -2\arctan\left(\frac{\sqrt{\sin^2\theta_{\mathrm{i}} - n^2}}{n^2\cos\theta_{\mathrm{i}}}\right) + \pi, & \theta_{\mathrm{i}} > \theta_{\mathrm{c}}, \end{cases} \tag{6}$$

$$\phi_{\mathrm{TE}} = \begin{cases} 0, & \theta_{\mathrm{i}} < \theta_{\mathrm{c}}, \\ -2\arctan\left(\frac{\sqrt{\sin^2\theta_{\mathrm{i}} - n^2}}{\cos\theta_{\mathrm{i}}}\right), & \theta_{\mathrm{i}} > \theta_{\mathrm{c}}, \end{cases} \tag{7}$$

where θ_{c} is the critical angle [$\theta_{\mathrm{c}} = \arcsin(n_2/n_1)$] when total internal reflection occurs. The phase shifts ϕ on the reflection

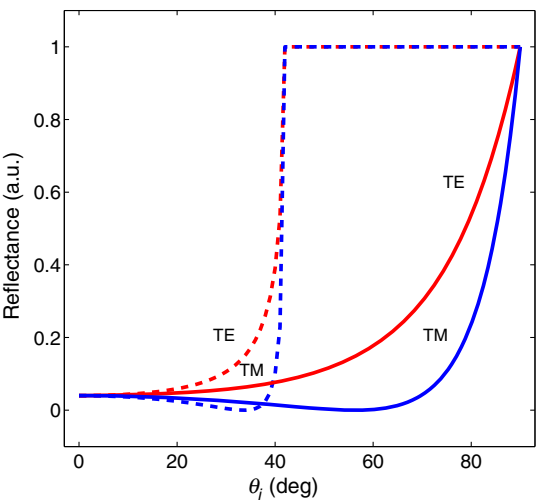

Fig. 1 Fresnel's reflection coefficients R_{TM} and R_{TE} for the external reflection, when $n_1 = 1.0$, $n_2 = 1.5$ (solid line), and for the internal reflection, when $n_1 = 1.5$, $n_2 = 1.0$ (dashed line), plotted as the functions of incidence angle θ_{i}.

for TE and TM modes depending on the angle of incidence are shown in Fig. 2.

Thus, considering superposition of light waves at the detector, the relative phase shift between m and v light waves due to their pathlength difference within the medium $(kS_{m,v})$, the phase shift due to reflection/refraction on the medium boundary $(\phi_{\mathrm{TE}}, \phi_{\mathrm{TM}})_{m,v}$, as well as the mutual phase shift due to variations of roughness heights from point to point

$$\Delta\phi(x,y)_{m,v} = \left(\frac{4\pi}{\lambda}\right)\Delta h_{\mathrm{rms}}(x,y)_{m,v}\ \sin\ \theta_i, \tag{8}$$

should be taken into account. Here, $\Delta h_{\mathrm{rms}} = h_m - h_v$ is the difference between m and ν root–mean-square heights, as shown in Fig. 3.

In the framework of this study, with the final aim to simulate the speckle patterns formation and to understand the role of surface roughness in the depolarization of linearly polarized light backscattered from turbid tissue-like scattering media, both the mutual phase shifts due to the pathlength difference within the medium and reflection/refraction on the rough surface of the medium were implemented into the electric field MC model.

2.2 *Electric Field Monte Carlo Modeling*

The principles of MC modeling of energy transfer through the medium are widely described elsewhere, see, e.g., Sobol.[21]

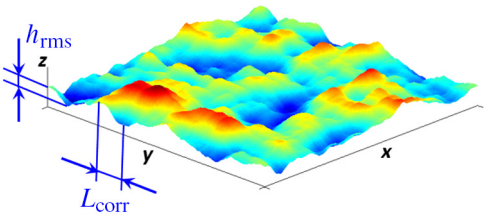

Fig. 3 Schematic presentation of randomly generated rough surface outlining and its key features, such as h_{rms} and correlation length L_{corr}, the parameters used for quantitative characterization of rough surfaces.[20]

Within the practical realization of this approach for modeling light propagation in the tissue-like scattering medium, a number of sophisticated techniques have been developed in the past[22–26] and used extensively in various applications in biomedical optics.[27] These MC models are based on the so-called scalar approach, i.e., when the incident light is assumed to be incoherent and not polarized. In these models, a photon packet is assigned with the initial weight and injected into a semi-infinite modeling medium. The injected photon packet undergoes a sequence of events representing light-tissue interaction, including scattering, absorption, reflection, and refraction at the medium boundary, until it is either fully absorbed or leaves the medium. At each event, the position of a photon packet is updated and its weight is reduced by a factor $e^{-\mu_t S}$, similar

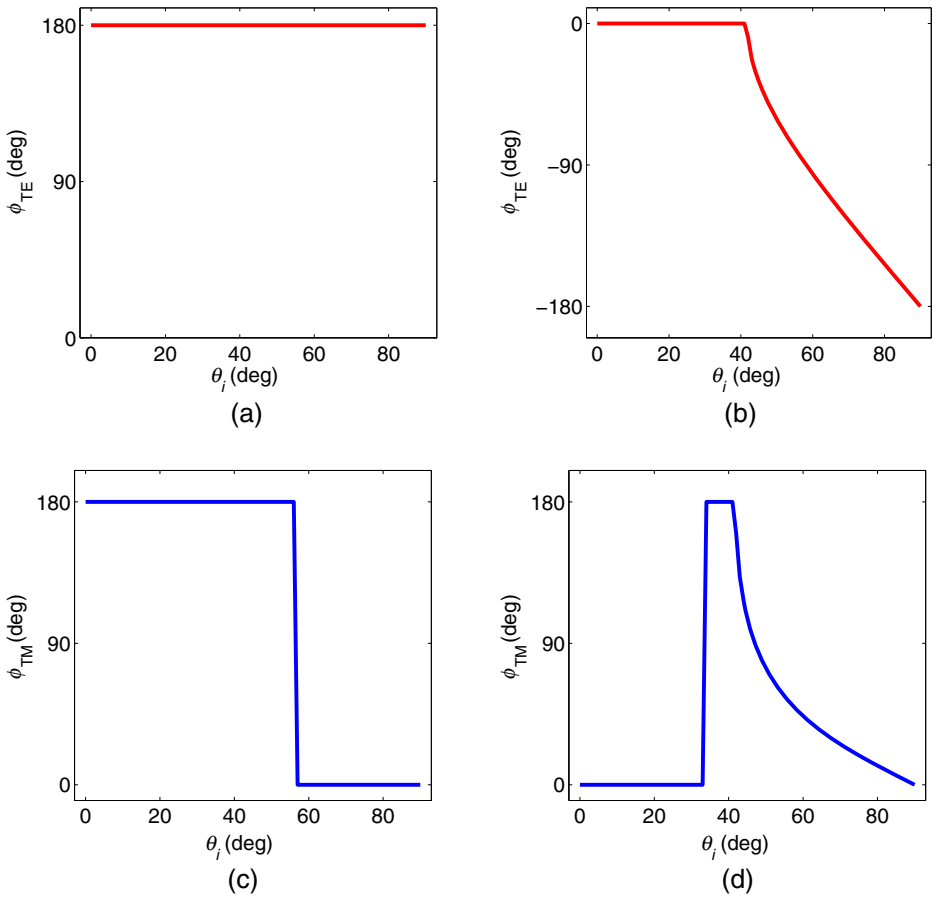

Fig. 2 Phase shifts on the reflection ϕ_{TE}, ϕ_{TM} depending on the angle of light incidence θ_i: (a) external and (b) internal TE reflection modes; (c) and (d) are, respectively, external and internal TM reflection modes, counted for the refractive indices: $n_1 = 1.0$, $n_2 = 1.5$.

to that described in Eq. (3). A new direction of the photon packet at a scattering event is defined by the Henyey–Greenstein phase function[28]

$$F_{\mathrm{HG}}(\theta) = \frac{1}{4\pi}\frac{1-g^2}{(1+g^2-2g\cos\theta)^{3/2}}, \tag{9}$$

where θ is the scattering angle ($\theta \in [0,\pi]$) and g is the anisotropy factor of scattering ($g \in [-1,1]$), defined as

$$g = \int_{-1}^{1} \cos\theta F_{\mathrm{HG}}(\cos\theta)\mathrm{d}\cos\theta.$$

Within further developments, several MC models have been developed to simulate the propagation of polarized light in scattering media.[29–35] Apart from the scalar MC mentioned above, the Jones[36,37] and Stokes–Mueller[38,39] formalisms are used in these so-called electric field MC models to describe and track the changes of a polarization vector along its propagation in the scattering medium.

In the electric field MC, utilized in this study, the Jones formalism[36,37] has been adopted to handle linear and/or circular polarization.[34,35] In the framework of this model, the photon packets, injected into the medium, are assigned with the statistical weight $W_0 = 1.0$ and with the initial polarization: $P_0 = [E_{0_x}, E_{0_y}, 0] = [1,0,0]$. Thestate of polarization at each scattering event is defined by a transform[40]

$$\vec{P}_i = -\vec{e}_i \times [\vec{e}_i \times \vec{P}_{i-1}] = [\hat{I} - \vec{e}_i \otimes \vec{e}_i]\vec{P}_{i-1}, \tag{10}$$

where $\vec{e}_i$ is the unit vector along the direction of propagation of the photon packet after $i-1$th scattering event, $\hat{I}$ is the unit forth-rank tensor, and $\otimes$ defines the vectors' multiplication.

Thus, the chain of projection operators $\hat{\mathbf{U}}_i$ transforms the initial polarization $\vec{P}_0$ upon a sequence of N scattering events to the final polarization $\vec{P}_N$

$$\vec{P}_N = \hat{\mathbf{U}}_N\hat{\mathbf{U}}_{N-1}\ \cdots\ \hat{\mathbf{U}}_1\vec{P}_0, \tag{11}$$

where $\hat{\mathbf{U}}_i = [\hat{I} - \vec{e}_i \otimes \vec{e}_i]$ is the tensor determined as

$$\hat{\mathbf{U}}_i = \begin{pmatrix} 1-e_{iX}^2 & -e_{iX}e_{iY} & -e_{iX}e_{iZ} \\ -e_{iX}e_{iY} & 1-e_{iY}^2 & -e_{iY}e_{iZ} \\ -e_{iX}e_{iZ} & e_{iX}e_{iZ} & 1-e_{iZ}^2 \end{pmatrix}. \tag{12}$$

Thereby, propagation of co- and cross-polarized components of the electric field within the scattering medium occurs along the trajectories counted by the scalar MC approach. According to the optical theorem,[41,42] the Rayleigh factor is taken into account at every scattering event to link the scalar and vector natures of the light wave[43,44]

$$\Gamma = \frac{2}{1+\overline{\cos^2\theta}}. \tag{13}$$

The reflection and refraction at the surface of the medium are taken into account by splitting the photon packet into transmitted and reflected parts.[45] Thus, the weights of a photon packet for TM and TE components after M reflections at the surface of the medium are defined as

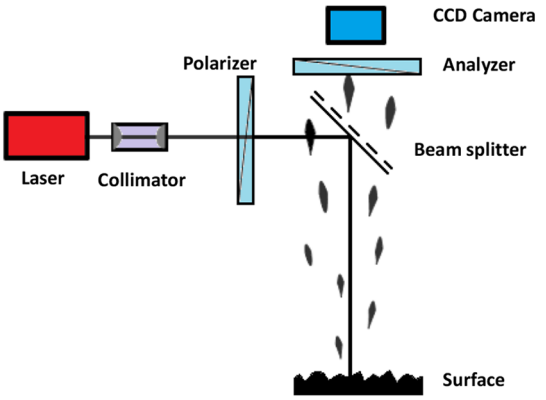

Fig. 4 Schematic presentation of the laser speckle imaging system used in the experimental studies.

Table 1 Optical properties of phantoms used in the experiment.

	μ_a (mm^{-1})	μ_s' (mm^{-1})	g
Phantom I	0.44 ± 0.04	0.51 ± 0.05	0.78 ± 0.01
Phantom II	0.26 ± 0.03	1.29 ± 0.13	0.67 ± 0.01

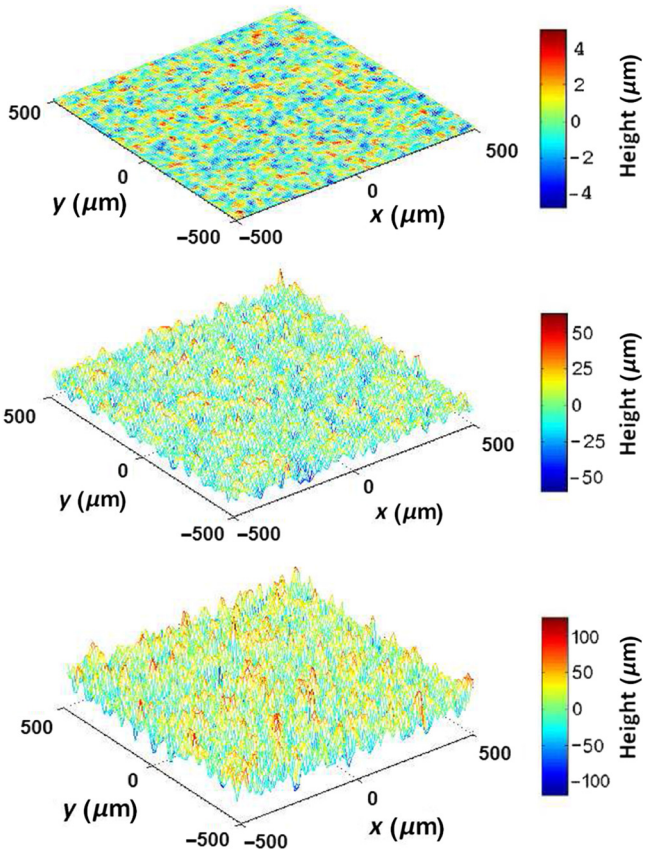

Fig. 5 The surface roughness profiles generated by the algorithm adopted from Tsang et al.,[48] from the top: h_{rms} are 2.5, 34.4, and 65.8 μm, and $L_{\mathrm{corr}} = 100$ μm for all profiles.

$$W(x,y)_{\mathrm{TM}} = W_0[1-R_0(x,y,\theta_{\mathrm{i}})_{\mathrm{TM}}]\left[\prod_{j=1}^{M-1} R_j(x,y,\theta_{\mathrm{i}})_{\mathrm{TM}}\right] \times [1-R_M(x,y,\theta_{\mathrm{i}})_{\mathrm{TM}}]P_{Nx}^2\Gamma^N \exp(-\mu_{\mathrm{a}}S),$$
$$W(x,y)_{\mathrm{TE}} = W_0[1-R_0(x,y,\theta_{\mathrm{i}})_{\mathrm{TE}}]\left[\prod_{j=1}^{M-1} R_j(x,y,\theta_{\mathrm{i}})_{\mathrm{TE}}\right] \times [1-R_M(x,y,\theta_{\mathrm{i}})_{\mathrm{TE}}]P_{Ny}^2\Gamma^N \exp(-\mu_{\mathrm{a}}S), \quad (14)$$

where $R(x,y,\theta_{\mathrm{i}})_{\mathrm{TM}}$ and $R(x,y,\theta_{\mathrm{i}})_{\mathrm{TE}}$ are the Fresnel coefficients [Eq. (5)].

Finally, the spatial distributions of co- and cross-polarized intensities ($I_{\parallel}$ and $I_{\perp}$) of the backscattered light in the far-field zone are counted as

$$I_{\parallel,\perp}(x,y) = \frac{1}{N_{\mathrm{ph}}}\sum_{m=1}^{N_{\mathrm{ph}}}(W_m + R_m)_{\mathrm{TM,TE}} + 2\sum_{m=1}^{N_{\mathrm{ph}}}\sum_{v}\left[\sqrt{R_m R_v}\cos(\Delta\phi_{m,v}) + \sqrt{R_m W_v}\cos(\phi_m+\alpha_v) + \sqrt{W_m W_v}\cos(\Delta\alpha_{m,v})\right]_{\mathrm{TM,TE}} \exp\left[-\left(\frac{\Delta L_{m,v}}{l_{\mathrm{c}}/\sqrt{2}}\right)^2\right], \quad (15)$$

and the DR is

$$\mathrm{DR}(x,y) = \frac{I_{\parallel}(x,y) - I_{\perp}(x,y)}{I_{\parallel}(x,y) + I_{\perp}(x,y)}, \quad (16)$$

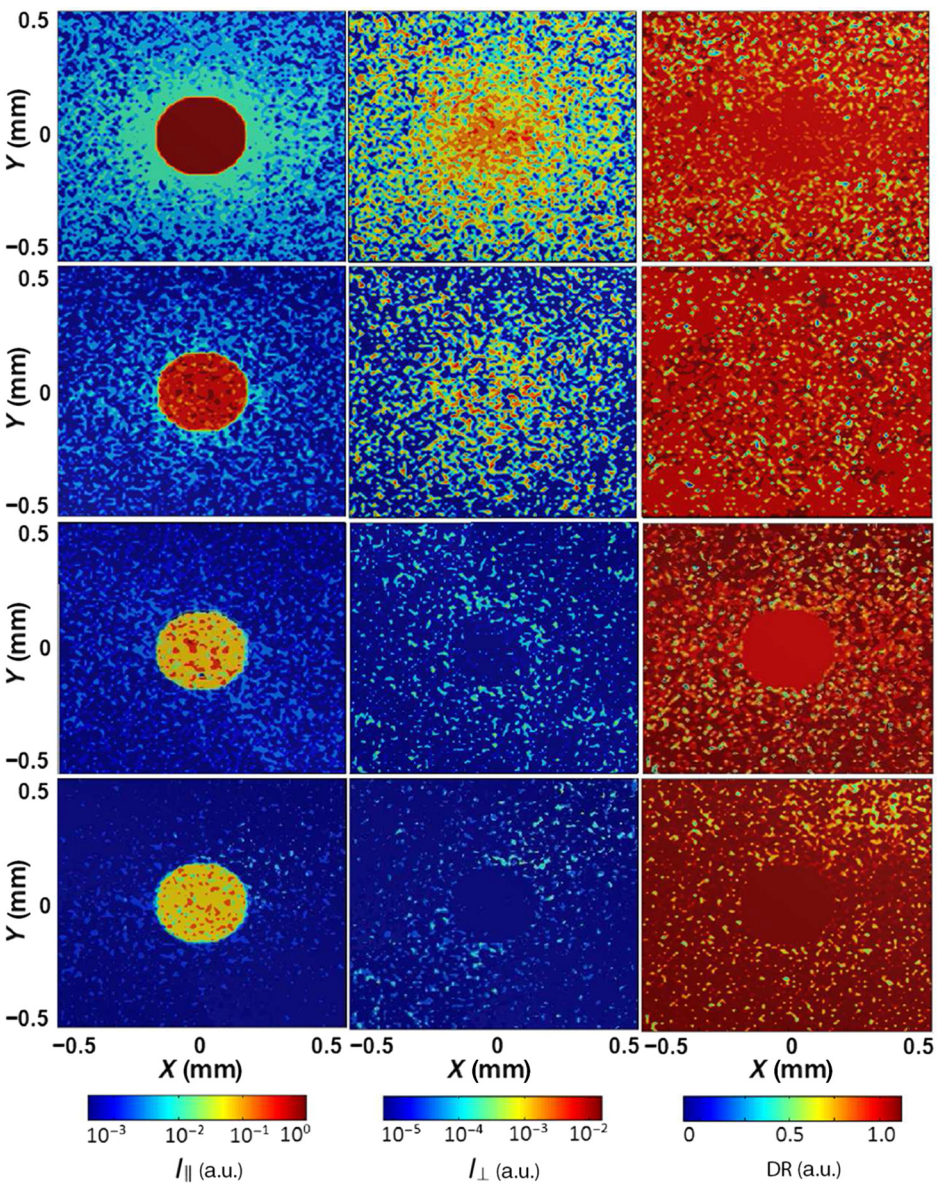

Fig. 6 Spatial intensity distributions of co- and cross- polarized light $I_{\parallel,\perp}(x,y)$ and depolarization ratio $\mathrm{DR}(x,y)$ counted for the modeling media with optical properties corresponding to the phantom I (see Table 1). The roughness from top row to bottom correspond, respectively, to $h_{\mathrm{rms}} = 0$, 2.5, 34.4, and 65.8 μm, and $L_{\mathrm{corr}} = 100$ μm.

where $R_{m,v}$ are the initial reflections at the surface of the medium at the area of illumination, $W_{m,v}$ are the weights of photon packets defined by Eq. (14). According to the experimental setup described below, detection of photon packets is considered in the far-zone with a narrow numerical aperture NA ~ 0.12, detection angle ≤ 7 deg.

Simulation of a large number of photon packets ($N_{\text{ph}} = 10^{11}$) is an intensive task and computational time has always been a significant concern in the MC models developed in the past. The MC model presented here has been developed utilizing the benefits and advantages of parallel programming offered by the compute unified device architecture (CUDA) on the NVIDIA graphics processing units (GPUs). The details of implementation of MC on CUDA NVIDIA GPUs for simulation of coherent polarized light propagation in the turbid scattering medium are given by Doronin et al.[34] The model's performance has been tested on the most recent Windows 10/Ubuntu GNU Linux 15.10 operating systems utilizing Tesla K80 parallel processors. For simulation of 10^{11} photon packets' trajectories, the modeling time takes $\sim$2 h for each surface roughness. The developed MC is a part of the computational tool available online[16,17] that has been extended for modeling of propagation and scattering of polarized light in turbid tissue-like scattering media.

3 Materials and Methods

Figure 4 schematically presents the experimental setup used for the MC model validation. A phantom with a rough surface is illuminated normally by a laser diode (5 mW, $\lambda = 663$ nm, $l_c = 30$ μm, Flex, B&WTek Inc.) with a 200 μm-diameter of the beam. The laser speckle patterns are observed by a CCD camera (Matrix Vision GmbH, mvBlueFOX-M124G—8 bit and mvBlueFOX-M224G—8 bit) utilizing a closed-circuit television (CCTV) lens (50 mm, $F/1.4$, Pentax Inc.). The polarizers (Thorlabs Inc., WP25L-UB) are used to control the input–output states of polarization. The Thorlabs pellicle beam splitter equally splits the co- and cross-polarized components without retardation. The processing of detected co- and cross-polarized images

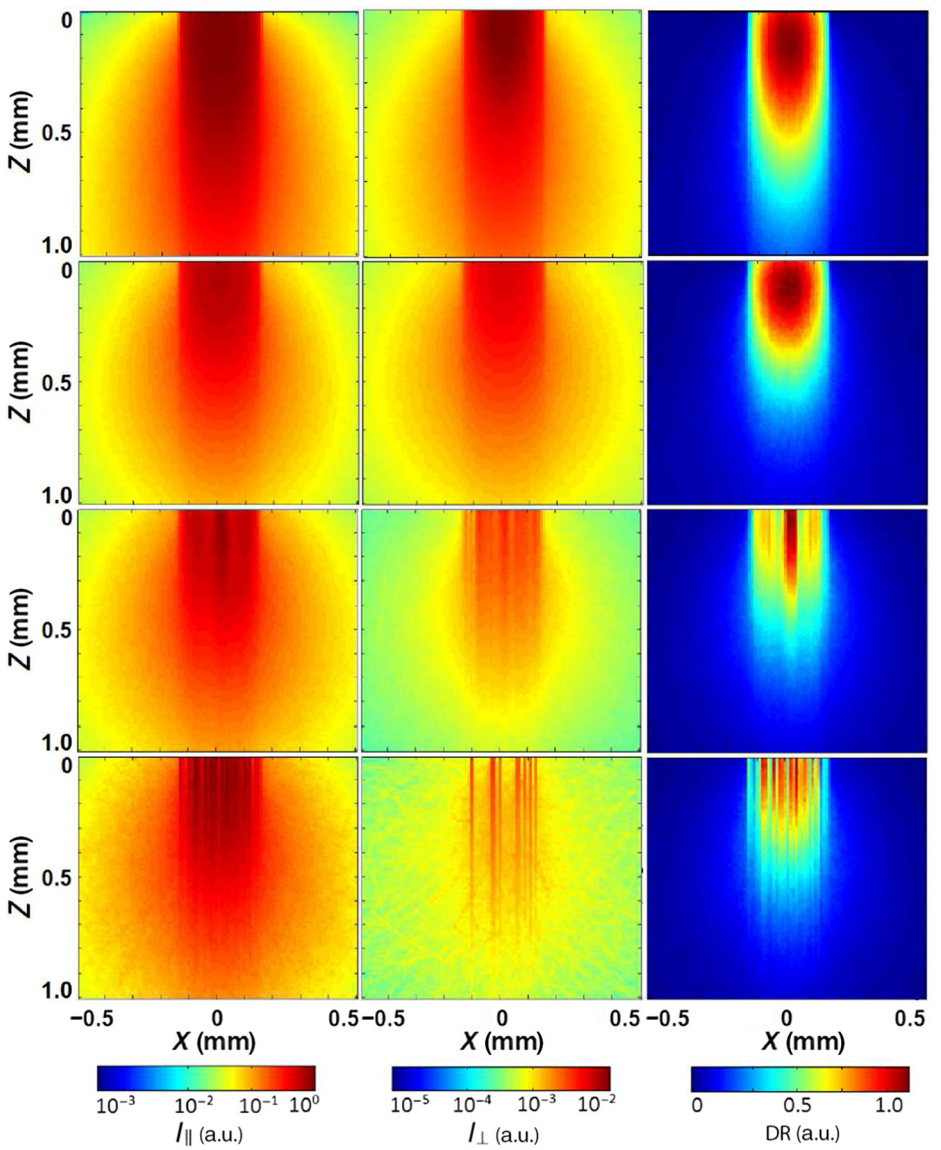

Fig. 7 Spatial intensity distributions of the detecting sensitivity along the depth for $I_{\parallel,\perp}(x, y)$ and their difference counted as DR for the media of the same properties, as presented in Fig. 6.

includes dark signal subtraction and accurate pixel-to-pixel correspondence adjustment. Spatial distribution of the DR is calculated by Eq. (16) utilizing spatial intensity distributions of co- and cross-polarized $[I_{\parallel}(x,y)$ and $I_{\perp}(x,y)]$ speckle patterns.

The phantoms used in the experimental studies have been prepared by utilizing silicone resin (the refraction index $n_R \approx 1.41$) with the embedded silicone pigments.[46] Optical properties of the phantoms were assessed by the standard integrated sphere-based approach,[47] utilizing a red diode laser (B&WTek Flex Inc.) presented in Table 1, where μ_s' is the reduced scattering coefficient,[40] defined as: $\mu_s' = \mu_s(1-g)$. The surface of phantoms used in the study has been replicated using metal standard (Microshurf #334, Rubert Co. Ltd.) with h_{rms} in the range from 10 to 66 μm and $L_{corr} = 100$ μm. This range of surface roughness parameters corresponds to the typical roughness of human skin.[47] The actual parameters of surface roughness of phantoms have been confirmed by measurements with the WYKO NT1100 optical profilometer (Veeco) providing vertical resolution 0.05 μm.

The standard algorithm[48] was adopted to generate profiles of the surfaces of the modeling media with the known roughness. In this algorithm, an uncorrelated Gaussian distribution of random numbers is generated. When convolved with the Gaussian filter, a series of points representing spatial distribution of points along the surface corresponding to the randomly selected values of h_{rms} are produced. Then generated values of h_{rms} are implemented into the surface as a mesh (see Fig. 3). Thus, the surface roughness profiles of modeling media presented in Fig. 5 were generated in accordance with the surface profiles of phantoms used in the experiment.

4 Results and Discussion

Spatial intensity distributions of co- and cross-polarized light $[I_{\parallel}(x,y)$ and $I_{\perp}(x,y)]$ and the DR counted with the electric

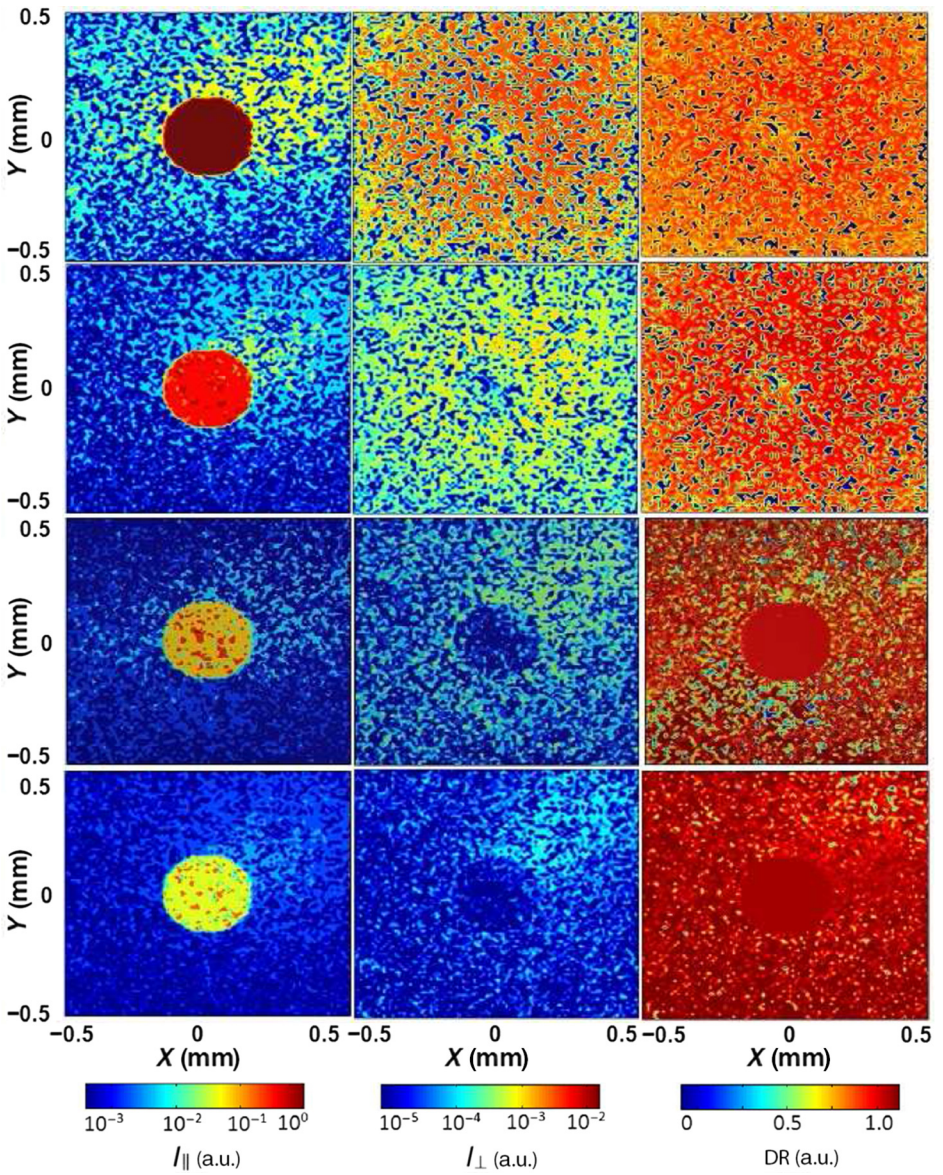

Fig. 8 Spatial intensity distributions of co- and cross-polarized light $I_{\parallel,\perp}(x,y)$ and depolarization ratio $DR(x,y)$ counted for the modeling media with optical properties corresponding to the phantom II (see Table 1). The roughness from top row to bottom correspond, respectively, to $h_{rms} = 0$, 2.5, 34.4, and 65.8 μm, and $L_{corr} = 100$ μm.

field MC approach described above are presented in Fig. 6. The optical properties of the medium are summarized in Table 1. The parameters of the rough surface are varied $h_{\mathrm{rms}} = 0$, 2.5, 34.4, 65.8 μm, and $L_{\mathrm{corr}} = 100$ μm.

The intensity of backreflected copolarized light $[I_{\parallel}(x,y)]$ in the area of illumination is dropped with the increase of h_{rms}, whereas the contrast of DR is increased. The reduction of $I_{\parallel}(x,y)$ is explained by the growing variability of incidence angle θ_{i} with an increase of h_{rms}. As a result in the far-zone within the fixed narrow detection angle (<7 deg), the Fresnel's reflection coefficients (see Fig. 1) and the phase shifts (due to reflection, see Fig. 2) become highly variable. Therefore, the intensities of co- and cross-polarized light $I_{\parallel,\perp}(x,y)$ are dropped as prescribed by Eqs. (14) and (15). Reflection from the medium surface is not contributing to the speckles' formation outside the area of illumination, therefore, the intensity distribution of $I_{\parallel,\perp}(x,y)$ is formed there only by the photon packets multiply scattered within the medium and experiencing internal reflection and refraction.

To illustrate the influence of surface roughness on the detected signal formation, Fig. 7 shows the spatial distributions of the detector depth sensitivity[49] for co- and cross-polarized components ($I_{\parallel}$ and $I_{\perp}$) and their difference, counted as an analogy of the DR [Eq. (16)]. The effective optical pathlengths S within the scattering medium counted by MC defines the paths that photon packets traveled within the medium from the point of incidence to the point of exit. Thereby, spatial distribution of the effective optical pathlengths within the medium can be considered in terms of the temporal point-spread function and this defines the detection sensitivity along the depth,[49] known also as a sampling volume.[50]

The results presented in Fig. 7 clearly show the influence of surface roughness on the detector depth sensitivity profile for co- and cross-polarized light ($I_{\parallel}$ and $I_{\perp}$), as well as their difference, defined by Eq. (16). The detector depth sensitivity is significantly reduced with the increase of h_{rms} (see Fig. 7), whereas the speckle patterns' contrast for $I_{\parallel}(x,y)$ and $I_{\perp}(x,y)$ with

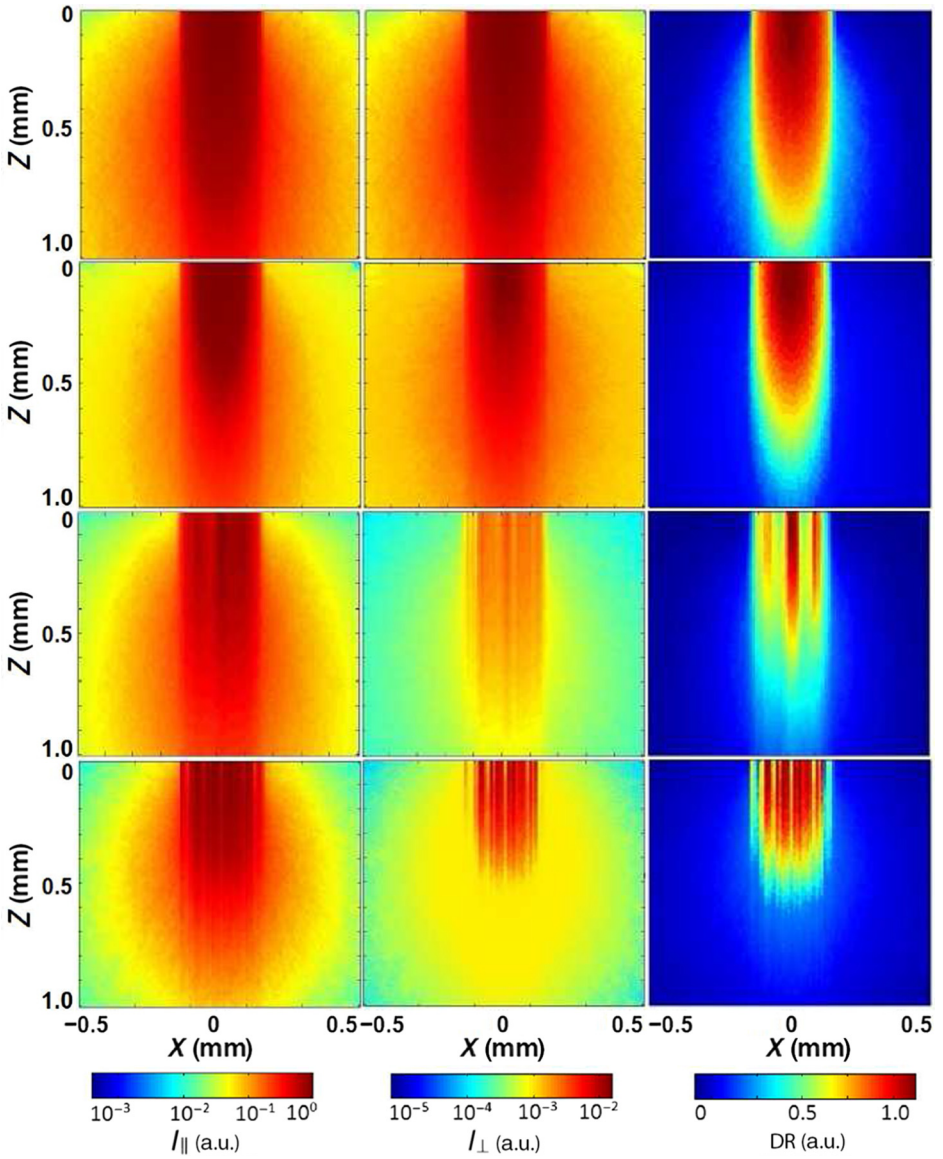

Fig. 9 Spatial intensity distributions of the detecting sensitivity along the depth for $I_{\parallel,\perp}(x,y)$ and their difference counted as DR for the media with the same properties, as presented in Fig. 8.

the higher values of h_{rms} becomes less comparable with the smoother surfaces (see Fig. 6).

In a similar manner, Figs. 8 and 9 show, respectively, the spatial intensity distributions and the detecting depth sensitivities for co-/cross-polarized light ($I_{\parallel}$, $I_{\perp}$) and DR counted for modeling media that are similar to the phantom II, with the same values of h_{rms} and L_{corr} (i.e., $h_{\mathrm{rms}} = 0$, 2.5, 34.4, 65.8 μm and $L_{\mathrm{corr}} = 100$ μm), and the optical properties presented in Table 1. As one can see with the same roughness spatial intensity distributions and detector depth sensitivity for $I_{\parallel,\perp}(x, y)$ and DRs are mainly influenced by optical properties of the scattering medium. Again, the bright circular spots seen at the copolarized $I_{\parallel}$ intensity distribution (see Figs. 8 and/or 9) correspond to the contribution of both specular reflection and diffuse reflection from the medium, although, for the cross-polarized light ($I_{\perp}$), the speckle patterns are formed mainly by the diffuse photons experienced internal reflection and refraction on the surface of the medium.

Bearing in mind that the results presented in Figs. 7 and 9 cannot be measured experimentally, to quantitatively compare the results of MC modeling and the results of experimental measurements of the spatial intensity distribution, we treated the speckle patterns utilizing second-order statistics.[46] In this approach, the spatial distributions of intensities $I_{\parallel,\perp}(x, y)$ are averaged along the selected radial distance d around the area of illumination as shown in Fig. 10.

Thus, by collecting the average intensities of co- and cross-polarized light ($\langle I_{\parallel}(d)\rangle$ and $lang; I_{\perp}(d)\rangle$) the DR is counted as

$$\mathrm{DR}(d) = \frac{\langle I_{\parallel}(d)\rangle - \langle I_{\perp}(d)\rangle}{\langle I_{\parallel}(d)\rangle + \langle I_{\perp}(d)\rangle}, \tag{17}$$

where $\langle \cdots \rangle$ denotes averaging along the distance (radius) d.

Radial distribution of the averaged DR [Eq. (17)] in terms of optical thickness $d/l*$ is presented in Fig. 11 in comparison with the results of experimental measurements for the phantoms I and II (presented in Table 1); $l*$ is the transport length ($l^* = 1/\mu_s'$) defining the length over which the direction of photon packet's propagation is randomized. The parameters of roughness used in the simulation for both phantoms are $h_{\mathrm{rms}} = 34.4$ μm and $L_{\mathrm{corr}} = 100$ μm.

As one can see, the results of the developed computational model agree well with the results of the experiment (see Fig. 11). Similar agreements were found between the results of modeling and the experiments for the phantoms with other roughness parameters, these are not presented here for brevity.

Figure 12 shows relative slopes of DR [Eq. (17)], averaged along radial distance in a similar manner as has been done in the experiment (see Fig. 10) and plotted as the result of normalized linear fit for the samples with different values of h_{rms}. The relative DR is an alternative representation of the results presented in Fig. 11 and apparently can be used as a quantitative measure of the relative changes of surface roughnesses.

5 Summary and Conclusions

Finally, with the further development of the unified computational model for the needs of biomedical optics and biophotonics,[16,17] we present the extension of the electric field MC for simulation of backreflectance and backscattering of coherent polarized light from turbid tissue-like scattering media with rough surfaces. The mutual phase shifts due to the pathlength difference within the medium and due to the reflection/refraction

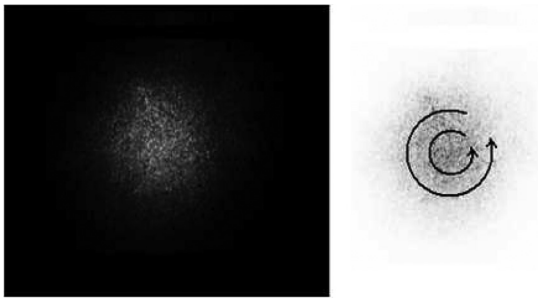

Fig. 10 The results of experimental measurements of $I_{\parallel}(x, y)$, raw data (left) and schematic presentation of the procedure of averaging along distances d around the area of illumination (right). The dimensions of the presented image are similar to those used in the simulation.

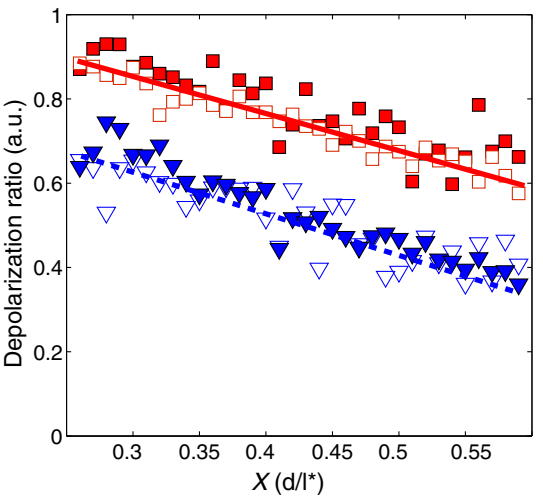

Fig. 11 Radial distribution of DR measured experimentally for the phantom I (□) and II (▽) in comparison with the results obtained by the electric field MC (■ and ▼). The solid and dashed lines represent the linear fits. The standard deviation for the results of experimental studies is in a range of 5–7%.

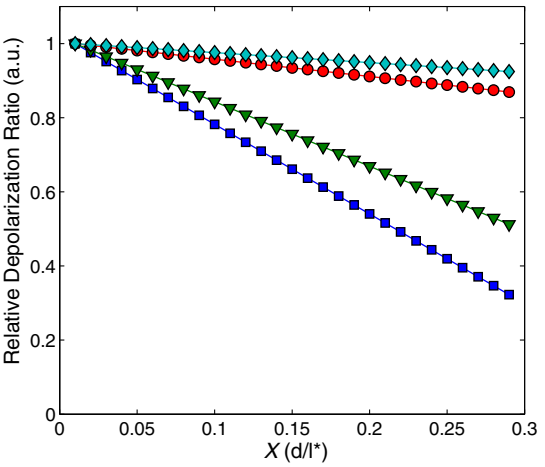

Fig. 12 Radial distribution of normalized DR plotted for the phantom I with $h_{\mathrm{rms}} = 0$ (■), $h_{\mathrm{rms}} = 2.5$ μm (▲), $h_{\mathrm{rms}} = 34.4$ μm (●), and $h_{\mathrm{rms}} = 65.8$ μm (◆).

on the rough surface of the medium are taken into account. The validation of the model includes the creation the phantoms of various roughness and optical properties, measurements of co- and cross-polarized components of the backscattered/reflected light, and its analysis and extensive computer modeling accelerated by the parallel computing on the NVIDIA GPUs using CUDA. To characterize the speckle patterns of the backscattered light, the spatial distribution of co- and cross-polarized light were measured/simulated and DR was analyzed taking into account radial symmetry. The DR was analyzed versus surface roughness for the phantoms for which the optical properties are of the same order as human skin lesions. The results of the computer modeling agree reasonably well with the results of experimental measurements. The developed computational approach allows straight modeling of speckle patterns' formation, their texture analysis, and, arguably, a quantitative assessment of surface roughness from the spatial distribution of the intensity of co- and cross-polarized scattering light. The analysis of the spatial intensity distribution is based on the second-order statistics that shows a strong correlation with the surface roughness, both with the results of modeling and experiment. The developed MC tool can be used for the direct simulation of light scattered by the tissue-like phantoms of various surface roughness. Further development of the model might include the periodic, anisotropic, and chiral surfaces as well as birefringent properties of the medium.

Acknowledgments

The authors acknowledge partial support provided by grants from the Canadian Dermatology Foundation, the Canadian Institutes of Health Research, the Natural Sciences and Engineering Research Council of Canada, UBC & VGH Hospital Foundation, and UBC Faculty of Medicine. The authors also acknowledge support provided by the Faculty of Information Technology and Electrical Engineering (ITEE) of the University of Oulu, Finland.

References

1. V. V. Tuchin, L. V. Wang, and D. A. Zimnyakov, *Optical Polarization in Biomedical Applications*, Springer, New York City (2006).
2. N. Ghosh and A. Vitkin, "Tissue polarimetry: concepts, challenges, applications, and outlook," *J. Biomed. Opt.* **16**(11), 110801 (2011).
3. A. Pierangelo et al., "Polarimetric imaging of uterine cervix: a case study," *Opt. Express* **21**, 14120–14130 (2013).
4. B. Kunnen et al., "Application of circularly polarized light for non-invasive diagnosis of cancerous tissues and turbid tissue-like scattering media," *J. Biophotonics* **8**, 317–323 (2015).
5. D. Bicout et al., "Depolarization of multiply scattered waves by spherical diffusers: influence of the size parameter," *Phys. Rev. E* **49**, 1767–1770 (1994).
6. A. H. Hielscher, J. R. Mourant, and I. J. Bigio, "Influence of particle size and concentration on the diffuse backscattering of polarized light from tissue phantoms and biological cell suspensions," *Appl. Opt.* **36**, 125–135 (1997).
7. L. F. Rojas-Ochoa et al., "Depolarization of backscattered linearly polarized light," *J. Opt. Soc. Am. A* **21**, 1799–1804 (2004).
8. V. L. Kuzmin and I. V. Meglinski, "Dependence of the circular polarization of backscattered light in random media on anisotropy of scatterers," *Opt. Spectrosc.* **108**, 99–106 (2010).
9. C. Brosseau, *Fundamentals of Polarized Light: A Statistical Optics Approach*, John Wiley, New York (1998).
10. A. Pierangelo et al., "Ex vivo characterisation of human colon cancer by Mueller polarimetric imaging," *Opt. Express* **19**, 1582–1593 (2011).
11. P. Ghassemi et al., "Out-of-plane Stokes imaging polarimeter for early skin cancer diagnosis," *J. Biomed. Opt.* **17**, 076014 (2012).
12. D. Gareau et al., "Automated detection of malignant features in confocal microscopy on superficial spreading melanoma versus nevi," *J. Biomed. Opt.* **15**, 061713 (2010).
13. M. C. L. Pacheco et al., "Implementation and analysis of relief patterns of the surface of benign and malignant lesions of the skin by microtopography," *Phys. Med. Biol.* **50**, 5535–5543 (2005).
14. P. R. Bargo and N. Kollias, "Measurement of skin texture through polarization imaging," *Br. J. Dermatol.* **162**, 724–731 (2010).
15. L. Tchvialeva et al., "Polarization speckle imaging as a potential technique for in vivo skin cancer detection," *J. Biomed. Opt.* **18**, 061211 (2012).
16. A. Doronin and I. Meglinski, "Online object oriented Monte Carlo computational tool for the needs of biomedical optics," *Biomed. Opt. Express* **2**, 2461–2469 (2011).
17. A. Doronin and I. Meglinski, "Peer-to-peer monte carlo simulation of photon migration in topical applications of biomedical optics," *J. Biomed. Opt.* **17**, 090504 (2012).
18. E. Wolf, *Introduction to the Theory of Coherence and Polarization of Light*, Cambridge University Press, Cambridge, United Kingdom (2007).
19. F. Pedrotti, L. Pedrotti, and L. Pedrotti, *Introduction to Optics*, 3rd ed., Prentice Hall, Upper Saddle River, New Jersey (2007).
20. M. Zerrad et al., "Gradual loss of polarization in light scattered from rough surfaces: electromagnetic prediction," *Opt. Express* **18**, 15832–15843 (2010).
21. I. Sobol, *The Monte Carlo Method*, The University of Chicago Press, Chicago, Illinois (1974).
22. B. Wilson and G. Adam, "A Monte Carlo model for the absorption and flux distributions of light in tissue," *Med. Phys.* **10**, 824–830 (1983).
23. S. Prahl et al., "A Monte Carlo model of light propagation in tissue," in *Proc. SPIE* **IS 5**, 102–111 (1989).
24. M. Keijzer et al., "Light distributions in artery tissue: Monte Carlo simulations for finite-diameter laser beams," *Lasers Surge. Med.* **9**, 148–154 (1989).
25. S. Feng, Z. Fanan, and B. Chance, "Monte Carlo simulations of photon migration path distributions in multiple scattering media," *Proc. SPIE* **1888**, 78–89 (1993).
26. L. Wang, S. Jacques, and L. Zheng, "MCML—Monte Carlo modelling of light transport in multi-layered tissues," *Comput. Meth. Prog. Bio.* **47**, 131–146 (1995).
27. C. Zhu and Q. Liu, "Review of Monte Carlo modeling of light transport in tissues," *J. Biomed. Opt.* **18**, 050902 (2013).
28. L. Henyey and J. Greenstein, "Diffuse radiation in the galaxy," *Astrophys. J.* **93**, 70–83 (1941).
29. X. Wang and L. Wang, "Propagation of polarized light in birefringent turbid media: a Monte Carlo study," *J. Biomed. Opt.* **7**(3), 279–290 (2002).
30. S. Gangnus, S. Matcher, and I. Meglinski, "Monte Carlo modeling of polarized light propagation in biological tissues," *Laser Phys.* **14**(6), 886–891 (2004).
31. J. Ramella-Roman, S. Prahl, and S. Jacques, "Three Monte Carlo programs of polarized light transport into scattering media: part I," *Opt. Express* **13**(12), 4420–4438 (2005).
32. J. Sawicki, N. Kastor, and M. Xu, "Electric field Monte Carlo simulation of coherent backscattering of polarized light by a turbid medium containing Mie scatterers," *Opt. Express* **16**(8), 5728–5738 (2008).
33. A. Radosevich et al., "Open source software for electric field Monte Carlo simulation of coherent backscattering in biological media containing birefringence," *J. Biomed. Opt.* **17**(11), 115001 (2012).
34. A. Doronin, C. Macdonald, and I. Meglinski, "Propagation of coherent polarized light in turbid highly scattering medium," *J. Biomed. Opt.* **19**, 025005 (2014).
35. A. Doronin et al., "Two electric field Monte Carlo models of coherent backscattering of polarized light," *J. Opt. Soc. Am. A* **31**, 2394–2400 (2014).
36. R. C. Jones, "A new calculus for the treatment of optical systems. I. Description and discussion of the new calculus," *J. Opt. Soc. Am.* **31**(7), 488–493 (1941).
37. H. Hurwitz and R. C. Jones, "A new calculus for the treatment of optical systems. II. Proof of three general equivalence theorems," *J. Opt. Soc. Am.* **31**(7), 493–499 (1941).
38. A. Gerald and J. M. Burch, *Introduction to Matrix Methods in Optics*, 1st ed., John Wiley & Sons, London (1975).

39. E. Collett, "Field guide to polarization," in *SPIE Field Guides*, Vol. **FG05**, SPIE, Bellingham, Washington (2005).
40. A. Ishimaru, *Wave Propagation and Scattering in Random Media*, Academic, New York (1978).
41. R. G. Newton, "Optical theorem and beyond," *Am. J. Phys.* **44**(7), 639–642 (1976).
42. P. S. Carney, E. Wolf, and G. S. Agarwal, "Statistical generalizations of the optical cross-section theorem with application to inverse scatter," *J. Opt. Soc. Am. A* **14**(12), 3366–3371 (1997).
43. V. Kuzmin and I. Meglinski, "Numerical simulation of coherent backscattering and temporal intensity correlations in random media (overview)," *Quantum Electron.* **36**, 990–1002 (2006).
44. V. Kuzmin and I. Meglinski, "Coherent effects of multiple scattering for scalar and electromagnetic fields: Monte-Carlo simulation and Milne-like solutions," *Opt. Commun.* **273**, 307–310 (2007).
45. D. Churmakov, I. Meglinski, and D. Greenhalgh, "Influence of refractive index matching on the photon diffuse reflectance," *Phys. Med. Biol.* **47**, 4271–4285 (2002).
46. L. Tchvialeva et al., "Enhanced diagnostic of skin conditions by polarized laser speckles: phantom studies and computer modeling," *Proc. SPIE* **8926**, 89260X (2014).
47. D. Diao et al., "Durable rough skin phantom for optical modeling," *Phys. Med. Biol.* **59**(2), 485–492 (2014).
48. L. Tsang, J. A. Kong, and K.-H. Ding, Scattering of electromagnetic waves: numerical simulations, in *Wiley Series in Remote Sensing*, Wiley-Interscience, Hoboken, New Jersey (2001).
49. I. V. Meglinski et al., "Study of the possibility of increasing the probing depth by the method of reflection confocal microscopy upon immersion clearing of near-surface human skin layers," *Quantum Electron.* **32**, 875–882 (2002).
50. I. V. Meglinski and S. J. Matcher, "Modelling the sampling volume for skin blood oxygenation measurements," *Med. Biol. Eng. Comput.* **39**, 44–50 (2001).

Alexander Doronin is a postdoctoral associate working in the Department of Computer Science, Yale University, United States. His research interests lie at the interface between computer science, physics, biomedical optics and biophotonics focusing on the development of algorithms for imitation of light propagation in scattering media such as human skin. Particular research areas include: Monte Carlo modeling of light transport, propagation and scattering of polarized light and Laguerre-Gaussian beams in turbid media, light-tissue interaction, physically-based rendering.

Lioudmila Tchvialeva is a lecturer in the Department of Physics at the University of British Columbia (UBC), Vancouver, Canada. She is also holding a researcher position in the Photomedicine Institute at the UBC Dermatology and Skin Science Department. Her research interests include propagation of coherent polarized light in turbid tissue-like scattering media, tissue polarimetry and applications of coherent light for diagnosis of skin deceases.

Igor Markhvida is an associate scientist at the British Columbia Cancer Research Centre (BCCRC), Vancouver, Canada. His research interests include coherent optics, speckle optics, biooptics, holography, Monte Carlo simulation and numerical techniques. He is author and coauthor of about 60 scientific papers and 8 patents.

Tim K. Lee is an associate professor in the University of British Columbia, senior scientist in the British Columbia Cancer Agency, and adjunct professor at Simon Fraser University, Canada. His research interests include skin cancer detection by using optical imaging. He developed polarization-based speckle technique for melanoma detection, skin surface roughness quantification, and algorithms for extracting and analyzing diagnostic features from dermoscopic and wide-area skin images. He is senior member of SPIE.

Igor Meglinski is a director of the opto-electronics and measurement techniques in the University of Oulu, Finland. His research interests include propagation of coherent polarized light in turbid tissue-like scattering media, coherent effects of multiple scattering of light, tissue polarimetry, angular momentum of light, optical phase singularities, dynamic light scattering, Monte Carlo modelling and multimodal imaging. He is a fellow of the Institute of Physics, London, United Kingdom, a senior member of IEEE and a fellow of SPIE.